Identifying Land Subsidence Using Global Digital Elevation Models

K. Becek[1*], K. Ibrahim[3], Ç. Bayık[2], S. Abdikan[2], H. S. Kutoğlu[2], D. Glabicki[1], and J. Blachowski[1]

[1]Wroclaw University of Science and Technology, Faculty of Geoengineering, Mining and Geology, Wroclaw, Poland.

[2]Zonguldak Bulent Ecevit University, Department of Geomatics Engineering, Zonguldak, Turkey.

[3]University of Brunei Darussalam, Faculty of Social Sciences, Brunei Darussalam.

[*]Corresponding author: Kazimierz Becek (kazimierz.becek@pwr.edu.pl)

ORCID: 0000-0003-1532-9725

Key Points:

- Land subsidence or uplift signals can be identified using digital elevation models.
- The difference between past and recent global digital elevation models reveals a land subsidence signal at the level of 20 mm yr^{-1}.
- Geoprocessing or an artificial intelligence approach can assist in identifying land deformations using dedicated software.

Abstract

Recent developments in space-based surveying methods of Earth's topography, including the differential synthetic aperture radar interferometry (DInSAR), increased the availability of options for monitoring of land subsidence. However, DInSAR methods require expert knowledge, specialized software, and are time-consuming. Here, we demonstrate that a land subsidence signal in the difference of freely available global digital elevation models (DEMs), e.g., SRTM and TanDEM-X, is identifiable using a simple statistical method. This finding opens up a venue to develop a dedicated computer application to identify land subsidence or uplift of the order > 20 mm yr^{-1}. Such an application would allow for the monitoring of the impacts of underground mining, earthquakes, landslides, volcanic activities, and similar effects on the Earth's topography. This software will provide a useful and cost-effective approach to scan the global DEMs for the benefit of many land planning and management agencies around the world.

Plain Language Summary

Land deformation is common throughout the globe and can potentially cause immense damage and loss. To monitor and manage incidences of land deformation, experts have developed a range of approaches that use spatial data about the Earth's surface captured by space-based satellites. However, most, if not all, of these approaches are costly and not readily available as they require expert knowledge, specialized software, and enormous amounts of time and other resources. Yet, we have found an alternative approach that uses freely available data in the form of global digital elevation models. By applying a simple statistical method that calculates differences in elevation of the same area between two considerably separate time periods, this approach can isolate and identify areas of rupture, movement or other forms of deformation of the Earth's topography as a result of natural events such as earthquakes and volcanic activities or human-made activities such as underground mining. By developing a suitable software application that uses this approach, the cost of detecting and monitoring land deformation can be significantly reduced, thus improving land survey and management efforts around the world.

1 Introduction

Underground mining has been attributed to several undesirable physical effects on the Earth's surface, including mining-induced land deformations and landslides. In populated areas, underground mining can interfere with the anthropogenic infrastructure, leading to extensive damage or destruction, and could endanger human safety. Some measures have been proposed to mitigate the impacts of mining. Still, the successful implementation of these measures depends on several factors, including financial constraints and local politics, as well as precise and updated information on the spatial extent and velocity of land deformation. The latter can be obtained thanks to recent developments in the spaceborne surveying methods of the Earth's surface, including the Synthetic Aperture Radar Interferometry (InSAR) (Crosetto & Pasquali, 2008; Rosen et al., 2000), Differential Synthetic Aperture Radar Interferometry (DInSAR) (Crosetto et al., 2000), Persistent Scatterers Synthetic Aperture Interferometry (PsInSAR) (Ferretti et al., 2000; Ferretti et al., 2001) and the Small Baseline Subset (SBAS) InSAR method (Berardino et al., 2002), which have significantly enriched the arsenal of surveying methods for monitoring and investigating land deformation. However, SAR interferometry-based methods require extensive computing resources and are time-consuming. In addition, these approaches

demonstrate some technical incompetence under certain circumstances when it comes to detecting surface deformations. For instance, they cannot detect the North-South deformation component, and create layover and shadowing problems that might also obstruct the results depending on the topography. Alternatives are therefore needed that are not only simpler in approach, more efficient and accurate, but also cost-effective in terms of the time required to process the data.

In this contribution, we demonstrate that freely available global digital elevation models (DEMs) can be used to identify land subsidence/uplift caused by mining activities. Our approach is based on comparing digital elevation models that were captured at two distant moments, during which time the deformation occurred. While this method is straightforward, it has perhaps deterred others from developing it further because of the limitations of the vertical accuracy of global DEMs on the order of a few meters and the magnitude of land deformations at the level of submeters, sometimes larger. Nevertheless, we have managed to develop this approach by performing the following tasks towards reaching the aim of this project:

- We developed a raster of mining-induced land deformation of a test area in Turkey using the SBAS (Berardino et al., 2002) method.
- Using regression analysis and hypothesis testing, we calculated the difference between the recent (2014) TanDEM-X DEM and the Shuttle Radar Topography Mission (SRTM) elevation data product as the reference dataset for the deformation and no-deformation regions.

Our calculations detected an identifiable signal in the differences between the DEMs, which strongly correlated with the land deformations. This finding provides a strong impetus for developing an application that can quickly and efficiently scan and calculate differences in existing global DEMs and identify land deformations of both anthropogenic and natural origins that have occurred during the first decade of the third millennia around the world.

2 Materials and Methods

2.1 Area of Interests (AOI)

The AOI is situated in the central northern part of Turkey. It borders the northern coastline of the Black Sea and covers an area of 17.7 km to the east and 11.5 km to the west. The geographic coordinates of the SW/NE corners of the AOI are (WGS84): (Lat/Lon): 41^{o}24’44”/ 31^{o}43’24” and 41^{o}31’04”/31^{o}56’05”. The topography is well developed. The average terrain elevation is approximately 233 m a.m.s.l. The lowest and highest points are at sea level and 600 m a.m.s.l., respectively. The dominant land cover (approximately 75 %) is forest, of which 90 % is comprised of the deciduous tree species.The coastal strip comprises of human settlements, including transportation and industrial infrastructure; the largest settlements are Zonguldak and Kozlu, with a total population of approximately 150,000 residents combined and are located in the western section of AOI. The largest industrial facility is a large power plant at Çatalağzı and located in the central north of the AOI. The main industry is underground mining of hard coal located underneath the Zonguldak and Kozlu towns and also in the central part of AOI. Mining has been conducted in the area for over 100 years (Arca et al., 2018). The mining operations have been carried out at a depth of 400 m to 600 m. Over the years, many land deformation and

landslide events have been observed, leading to serious damage to properties and even to deaths (Arca et al., 2018).

2.2 Data

2.2.1 Shuttle Radar Topography Mission (SRTM) Digital Elevation Data Product

The SRTM-1" (v.3) (SRTM) elevation data product is a well-known global DEM that has been used for many types of geospatial studies in several branches of science. The space shuttle "Endeavor" in February 2000 hosted the unique single-pass Synthetic Aperture Radar (SAR) instrument to acquire the data for processing using the SAR interferometry (InSAR) method to generate semi-global DEM. The SRTM data product is available at one- and three-arcsec resolution (approximately 30 m or 90 m at the Equator). The three-arc second version was produced by the averaging process of the original one arc-second model. The vertical accuracy of SRTM DEM is approximately 2 m (one sigma - for horizontal surfaces), which is well over the mission's requirement (Rabus et al., 2003; Becek 2008, 2014). Version 3 of the SRTM-1" is used as a reference data set in this contribution. The horizontal reference system used is WGS84, and the elevation is provided with reference to the Earth Gravity Model (EGM96). As the data for the SRTM product was captured during the winter season in the northern hemisphere, the deciduous forests were in the leaves-off state, allowing for partial penetration of vegetation by the C-band microwaves of the SRTM mission SAR system (Becek, 2011).

2.2.2 TanDEM-X Digital Elevation Data Product

TanDEM-X 30m DEM (TDX) is an elevation data product developed from the data captured by the TerraSAR-X/TanDEM-X mission (Krieger et al., 2007). Similar to the SRTM, the TDX is a quasi-DSM representing the elevation of the terrain, including objects above the ground and elevation of the phase center between the canopy and the terrain in vegetated areas (Becek, 2011). The spatial resolution of the TDX models is one arcsec or approximately 30 m at the Equator. This model was developed by one of the authors of the paper using bilinear resampling of 0.4 arcsec resolution data provided by DLR as a part of a research project. However, the TanDEM-X DEM can be downloaded at the 3" arcsec resolution from https://geoservice.dlr.de/web/dataguide/tdm90/ free of charge. The 0.4 arcsec DEM is available as a commercial product known as WorldDEM™ (Becek et al., 2016). The vertical accuracy of the TDX is approximately 2 m (one sigma), while the accuracy of the WorldDEM™ is approximately 0.8 m (one sigma) (Becek et al., 2016). Since the source of the data for the TDX and WorldDEM™ are the same, one can expect that the conclusions from this study are valid for both models. The horizontal reference system for TDX is WGS84. The vertical datum is the WGS84 ellipsoid. According to the metadata file of the TDX, the SAR data were acquired during 27 passes of the satellites between 17/02/2011 and 27/08/2014 and then averaged. Fifteen images were taken during the leaves-off state of vegetation (autumn to early spring). This further means that a vegetation bias can be present in the TDX and be similar to that of SRTM.

2.2.3 Synthetic Aperture Radar (SAR) Data

To identify the deformations in AOI, we used the SAR data captured by the Copernicus Sentinel 1A/B satellite mission (ESA, 2020). A total of 103 images acquired in the Interferometric Wide-Swath (IW) mode from the descending orbit no. 65 were used in the study. The images were acquired between Jan. 2018 and Oct. 2019.

147 2.2.4 Reference DEM

148 A high quality and recent DEM model (HQM) was used to calibrate the SRTM and TDX
149 models. The HQM is a digital surface model (DSM) produced from stereo pairs of 2017 aerial
150 photography. The original DSM was produced at the resolution of 0.45 m, but it was available to
151 the authors at the resolution of 5 m. The vertical accuracy is 1.52 m (one sigma) (Yilmaz &
152 Erdoğan, 2018). The HQM is referenced to the national heighting system of Turkey (orthometric
153 system). The HQM was further downsampled using the bilinear method to one arcsec resolution
154 as the investigated DEMs. The assessment of the vertical accuracy of the model was confirmed
155 using the runway method [4], carried out at a few selected flat sites, including sports fields and a
156 highway.

157 2.3 Methods

158 2.3.1 Small Baseline Subset (SBAS) method

159 The SBAS method is a version of the Differential SAR interferometry (DInSAR) method,
160 (e.g., Lanari et al., 2007). The SBAS method was developed to monitor land deformation as a
161 function of time (Berardino et al., 2002). This method allows for the estimation of the velocity of
162 the deformation with an accuracy of approximately 5 mm yr-1 (Casu et al., 2005, 2006; Lanari et
163 al., 2007). The SBAS data processing procedure has been described by others (e.g., Ferretti et al.,
164 2001; Hanssen, 2001; Rosen et al., 2000) and its applications include assessing land subsidence
165 under big cities (Amelung et al., 1999; Lanari et al., 2004), monitoring land subsidence caused
166 by groundwater level change (Normand & Heggy, 2015), monitoring volcano eruption (Lee et
167 al., 2006), and assessing mining-induced land deformation (Goel & Adam, 2014). One of the
168 initial SBAS processing steps is to form the interferograms based on pairs of images taken from
169 different points on the orbit separated by the spatial baseline. The second condition for selecting
170 the images for interferogram is to restrict the temporal baseline (time between two image
171 acquisitions). A temporal baseline of shorter than 36 days and a spatial baseline shorter than 100
172 m were adopted in our case. Given the conditions, a total of 326 interferograms were formed.
173 The SRTM-1" DEM was used to subtract the topographic phase from interferograms - a step in
174 the SBAS data processing. As a final result, the raster of the Line-of-Sight (LOS) deformation
175 had been obtained. The LOS deformation is a composite vector of land subsidence and
176 horizontal displacement. Since we processed the images from the descending orbit only, it is not
177 possible to split the LOS vector into the north/east components. The resulting raster has a spatial
178 resolution of approximately four arcsec. The interferometric calculation, as well as the SBAS
179 processing, were performed in the GMTSAR software (Sandwell et al., 2011). The SNAPHU
180 software was used to unwrap the interferograms (Chen & Zebker, 2001).

181 2.3.2 Vertical Accuracy Model of the DEMs Difference

182 The vertical accuracy statement of the DEMs provided in Sections 2.2.1 to 2.2.4 covers
183 the instrument- and the environment-induced component of the elevation error only (Becek
184 2008, 2014). These components do not include the contribution of the so-called target induced
185 component, which depends on the size of the pixel and slope of the terrain. The contribution of
186 these two variables can be calculated from Equation (1) (Becek 2008):

187 $$\sigma^2 = \frac{1}{12} d^2 tan^2(s), \quad (1)$$

where σ^2 is the variance of the target-induced error,

d is pixel size, and

s is the slope at a given pixel.

The target-induced error of a DEM for a given AOI is the arithmetic average of the errors of all pixels within the AOI.

To calculate the total vertical error of a DEM within a given AOI, we assume that the components of the error, e.g., the instrument-, environment-, and target-induced errors are statistically independent. Hence, the total vertical error can be estimated using Equation (2) [ibid]:

$$\sigma_{total}^2 = \sigma_I^2 + \sigma_E^2 + \sigma_T^2, \quad (2)$$

where $\sigma_I^2, \sigma_E^2, \sigma_T^2$ are the variance of the instrument-, environment- and target-induced error.

In further considerations, we omitted the environment-induced error. In this study, we used the difference between the DEMs. To estimate the vertical error of the difference of two uncorrelated random variables (DEM_1 and DEM_2), we used the error propagation law expressed in a simple form as per Equation (3):

$$\sigma_{diff}^2 = \sigma_{DEM1}^2 + \sigma_{DEM2}^2, \quad (3)$$

where $\sigma_{diff}^2, \sigma_{DEM1}^2, \sigma_{DEM2}^2$ is the variance of the error of difference, DEM_1, and DEM_2, respectively.

Note that we used here the term ‘variance’ as the second power of the ‘standard deviation.’ However, in a more general case, when there is a bias or systematic error in the difference between random variables (avg(DEM_1 - DEM_2) <> 0), the correct term is the ‘mean squared error’ or MSE.

3 Results

3.1. Line-of-Sight (LOS) Deformation

Figure 1 shows a map of the LOS deformations in the AOI calculated for the period between January 2018 and October 2019. The locations of some of the mines (red solid line) are also shown on the map. The deformations appear to be closely associated with underground mining operations. In the northeastern and southern sections of the map, some uplift areas are visible. Avsar et al. (2017) suggest a tectonic uplift of up to 6 mm yr^{-1} around the Black Sea region as a possible reason. In addition, the artifacts related to the low coherence may be due to vegetation.

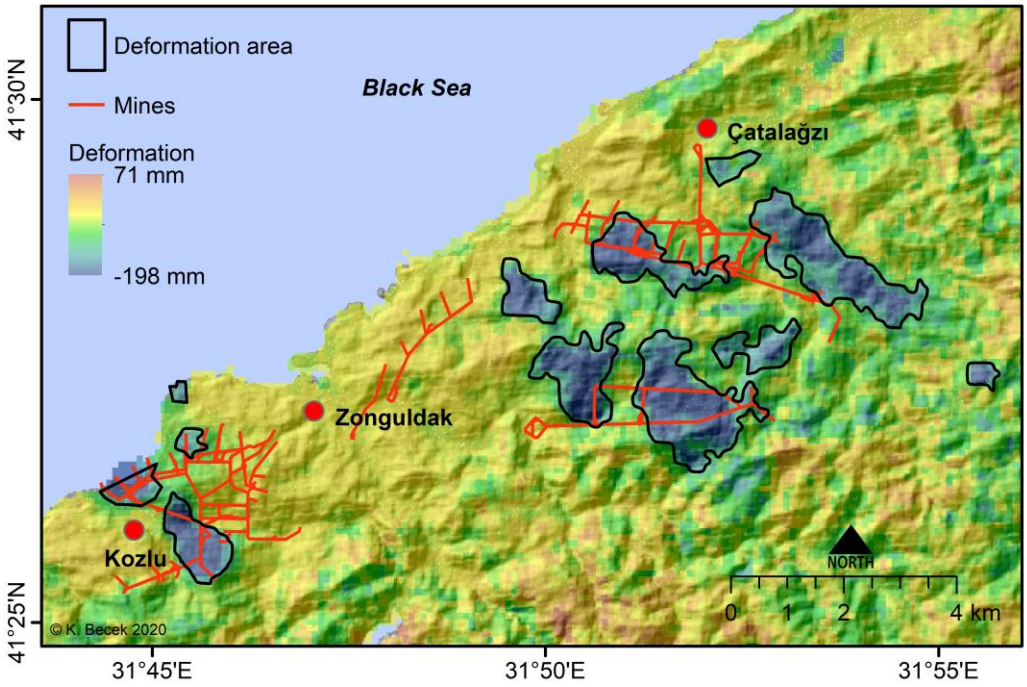

Figure 1 The Line of Sight (LOS) raster of deformation as a result of SBAS processing of the Copernicus Sentinel 1A/B SAR data. The deformations occurred between January 2018 and October 2019. The approximate location of the mining infrastructure is also shown.

The deformation areas were manually, and arbitrary outlined (solid black line). Figure 2 shows histograms of deformations for the deformation (a), and no-deformation areas (b), respectively. The histograms are bimodal (negative skew), suggesting that two random processes are contributing to the deformations. The histograms were modeled using the generalized Gaussian pdf. The analysis of the histograms helps to identify the origin of the underlying processes contributing to the deformation. Hence, the Gauss 1 and Gauss 3 curves in Figure 2 represent the measurement noise of the SBAS technique. Since the Gauss 1 curve also contains some residuals of the deformation signal, its standard deviation (10.8 mm) is higher than that of the Gauss 3 curve. This conclusion is consistent with the results found in, e.g., (Casu et al., 2005, 2006; Lanari et al., 2007).

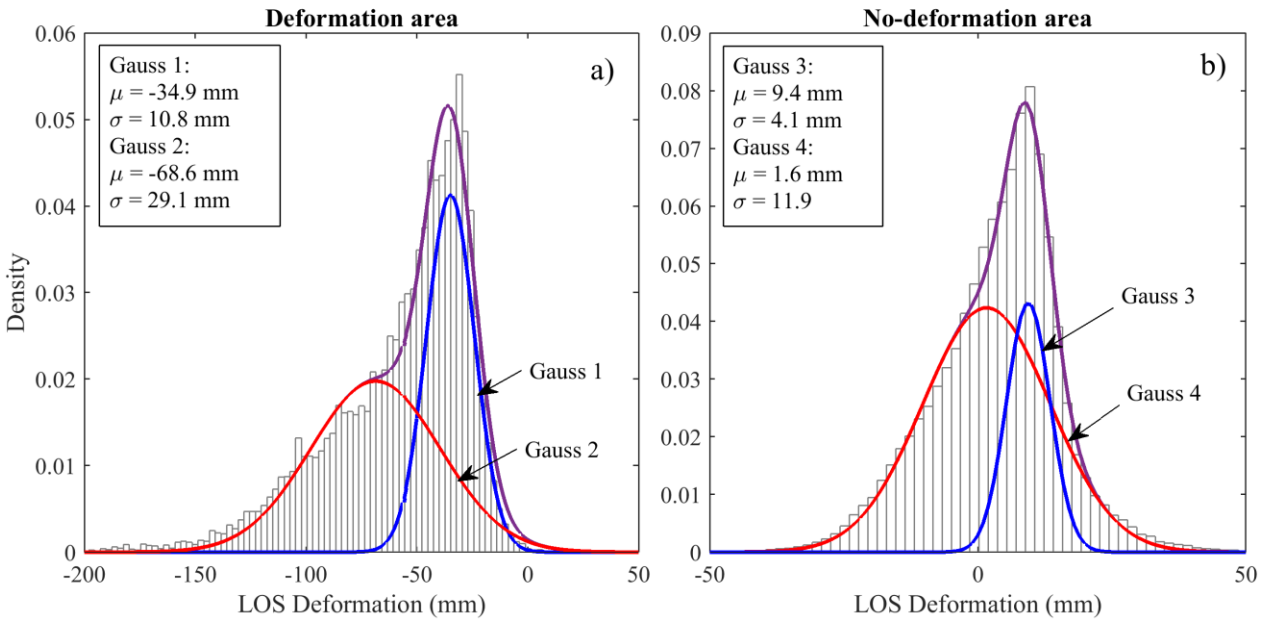

Figure 2 Histograms of the LOS deformation in a) the deformation area, and b) the no-deformation area Histograms are modeled using a two-term generalized Gaussian pdf. The mean and standard deviation are also shown. The negative skewness of the histogram indicates the presence of land subsidence in the AOI.

The curve Gauss 2 in Figure 2a represent the deformation in the deformation area. It reveals that the average deformation is -68.6 mm with the standard deviation of 29.1 mm, which translates to –3.4 mm yr^{-1}.

3.2. DEMs difference

The TDX and SRTM models exhibit elevation bias with respect to the local orthometric vertical reference systems. The source of this bias may be related to the calibration of SAR instruments, the precision of the EGM96 geoid model, and the characteristics of the local heighting system. Depending on the region of the world, the bias may be negative or positive and is of the order of one meter (Becek, 2014). To remove the bias from TDX and SRTM, we used a reference HQM. We corrected the DEMs by subtracting the average difference between both models and HQM with the opposite sign. We found that the bias for the TDX (including the geoid undulation) was 32.38 m (TDX was too high); the SRTM bias was -1.524 m (SRTM was too low). Figure 3 shows a map of differences between the (corrected) TDX and SRTM.

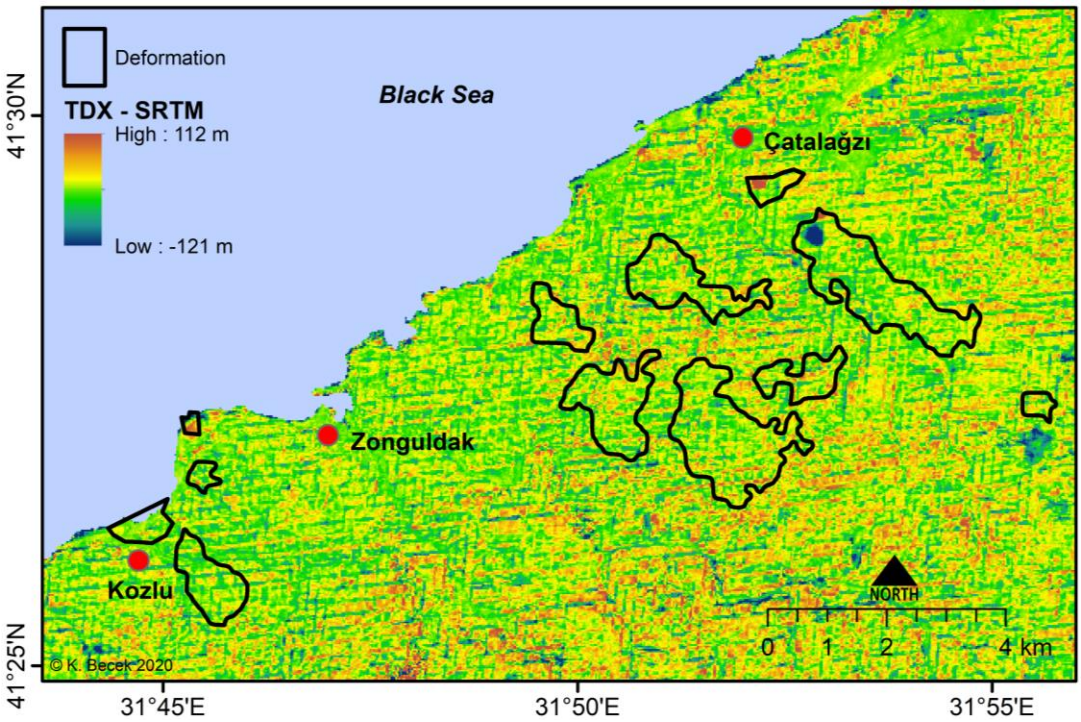

Figure 3. Map of the difference TDX *minus* SRTM. The SBAS-estimated location of deformation areas is also shown.

The histograms of the difference between the corrected TDX *minus* SRTM models are shown in Figure 4. We performed the one-sample Kolmogorov-Smirnov test to verify the hypothesis that the differences follow a normal distribution. The result suggests that the differences do not follow a normal distribution at the 5% significance level. Instead, we use the Laplace probability density function (pdf) to model the histogram. The Laplace pdf is controled by μ - the location parameter and b - the scale parameter. The maximum likelihood estimator of μ is the sample median, and the estimator of b is the mean absolute deviation from the location parameter (Robert & Norton,1984). The variance of difference is $\sigma^2 = 2b^2$.

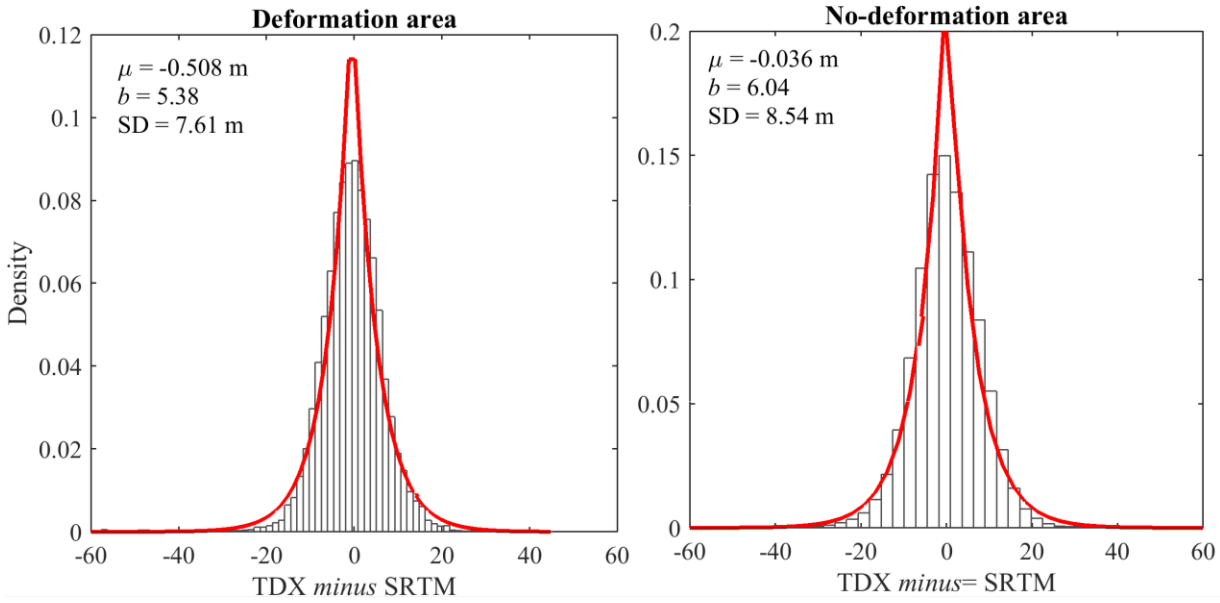

Figure 4. Histograms of differences between TDX *minus* SRTM for the deformation and no-deformation areas. The Laplace pdf curves, including the location parameter (μ), scale parameter (*b*), and the standard deviation (SD, for the deformation (a) area, and no-deformation area (b) are also shown.

The calculations yielded the location parameter (approximate average difference) = -0.508 (σ = 7.61) m, and -0.036 (σ = 8.54), for the deformation and no-deformation area, respectively.

The average difference in the deformation area is smaller than in the no-deformation area by -0.472 m (= -0.508 + 0.036), suggesting that TDX contains the deformation signal or anomaly. To verify if this observation is statistically significant, we conducted a hypothesis test. The null hypothesis is (H_0): The average difference TDX *minus* SRTM $\mu = 0$ m. The alternative hypothesis is H_A: The average difference $\mu < 0$ m. To perform the test, we randomly selected 1000 pixels in the no-deformation area. The mean difference for these random points was -0.495 m (s = 7.78 m). We found the *p*-value = 0.025 < 0.05 or the confidence level of 95%. These results allows us to reject the null hypothesis at the 95% confidence level, which means that the difference TDX *minus* SRTM within deformation and no-deformation areas are statistically significant.

3.3 Difference vs. Deformation

Figure 5 shows a scattergram of the difference TDX *minus* SRTM vs. LOS deformation. A linear trend suggests a relationship between both variables. The Spearman's correlation test for the deformation area produced correlation coefficient = 0.045 with *p*-value = $5.2231*10^{-9} < 0.01$.

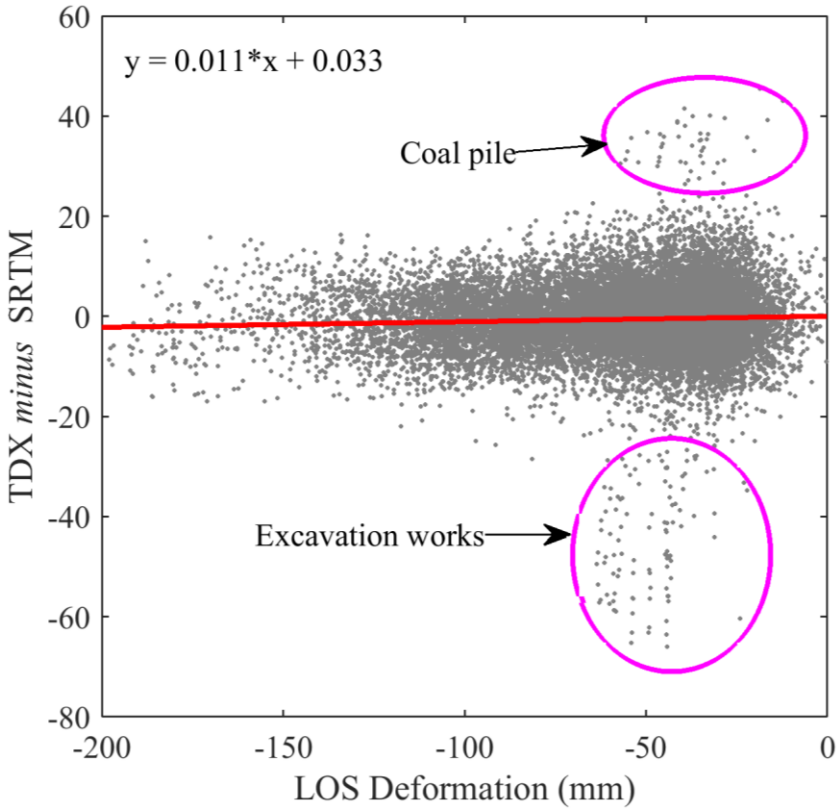

Figure 5. TDX *minus* SRTM vs. LOS deformation, including a regression line. The correlation coefficient = 0.045, *p*-value = $5.2231*10^{-9} < 0.01$ (Spearman's test).

The pink ellipses in Figure 5 delineate outliers (that were considered in the hypothesis tests). A detailed inspection of the outliers determined that they are not related to the land deformation, but to the open pit excavations and piling of a byproduct of the coal power plant at Çatalağzı.

4 Conclusions

To the authors' knowledge, this is the first study to use the global digital elevation models to identify land deformations of the order of a few cm yr^{-1}. It is a straightforward approach for which the basic requirement is that there be a sufficient period between when selected DEMs were captured. In our case, the lapse is approximately ten years. As a test field, we used a region exposed to long-term underground mining-induced land deformation. Still, this approach could be applied to identify any other type of deformations, either uplift or subsidence. The causes of land deformation may include tectonic-, seismic-, landslides-, and volcanic-induced topography change over time. Since the LOS deformation occurred within a 20-month period, the average velocity = -68.6 mm over 20 months or -41.2 mm yr^{-1}. Considering this value in the context of the average difference between TDX and SRTM, which is approximately -472 mm and appeared over approximately 168 months or -33.7 mm yr^{-1}, one can conclude that the results are consistent (the vertical component of the LOS deformation vector is smaller than the LOS vector).

The sensitivity of this method to identify land deformation depends on the accuracy of the DEMs used. A key and variable component of the accuracy of a DEM is the target-induced error (see Equation 1), which depends on the pixel size and local slope. This fact justifies the statement that for a given pair of DEMs (e.g., SRTM and TDX), the sensitivity of the method depends on the roughness of terrain: Higher slopes limit the sensitivity of the technique. The average slope in our case was 12.4°.

We have also tested the AW3D30 m DEM (Tadono et al., 2016) against SRTM. The obtained results (not shown here) were similar, suggesting that other DEMs can be used for similar studies of land deformations anywhere in the world.

To conclude, this paper has proven the effectiveness of this method to detect land deformation using readily available DEMs. By developing a dedicated software using artificial intelligence that implements this technique, it is possible to save time and costs to construct the DInSAR-based deformation raster.

Acknowledgments, Samples, and Data

The authors declare no and real or perceived financial conflict of interest.

The authors are grateful to Prof. Manfred Buchroithner for his helpful comments. Datasets for this research are available in Becek et al., (2020).

References

Amelung, F., Galloway, D. L., Bell, J. W., Zebker, H. A., & Laczniak, R. J. (1999). Sensing the ups and downs of Las Vegas: InSAR reveals structural control of land subsidence and aquifer-system deformation. *Geology*, *27*(6). 483–486. https://doi.org/10.1130/0091-7613(1999)027<0483:STUADO>2.3.CO;2

Arca, D., Kutoğlu, Ş. H., & Becek, K. (2018). Landslide susceptibility mapping in an area of underground mining using the multicriteria decision analysis method. *Environmental Monitoring and Assessment*, *190*(12). https://doi.org/10.1007/s10661-018-7085-5

Avsar, N. B., Jin, S., Kutoğlu, Ş. H., & Gurbuza, G. (2017). Vertical land motion along the Black Sea coast from satellite altimetry, tide gauges and GPS. *Advances in Space Research*, 60(12), 2871-2881.

Bayık, C., Becek, K., Mekik, C., & Ozendi, M. (2018). On the vertical accuracy of the ALOS world 3D-30m digital elevation model. *Remote Sensing Letters*, *9*(6), 607–615. https://doi.org/10.1080/2150704X.2018.1453174

Becek, K. (2008). Investigating error structure of shuttle radar topography mission elevation data product, *Geophysical Research Lett*ers. *35*, L15403. https://doi.org/10.1029/2008GL034592

Becek, K., Koppe, W., & Kutoğlu, Ş. H. (2016). Evaluation of vertical accuracy of the WorldDEM™ using the runway method. *Remote Sensing*, *8*(934). https://doi.org/10.3390/rs8110934

Becek, K. (2011). *Biomass representation in synthetic aperture radar data sets: a comprehensive study of biomass-induced elevation bias in DEMs derived using synthetic aperture radar interferometry*. Saarbrucken, LAP Lambert Academic Publishing.

Becek, K. (2014). Assessing global digital elevation models using the runway method: The advanced spaceborne thermal emission and reflection radiometer versus the shuttle radar topography mission case. *IEEE Transaction on Geoscience and Remote Sensing, 52*(8), 4823–4831. https://doi.org/10.1109/TGRS.2013.2285187

Becek, K., Kutoğlu, Ş. H., Glabicki, D., Bayık, C., Blachowski, J., & Abdikan, S. (2020). Zonguldak, Turkey: Mining-induced land deformation in 2018-2019 - Sentinel 1 SBAS results. Mendeley Data, v1, https://doi.org/10.17632/szhw6k2bsv.1

Berardino, P., Fornaro, G., Lanari, R. & Sansosti, E. (2002). A new algorithm for surface deformation monitoring based on small baseline differential SAR interferograms. *IEEE Transaction on Geoscience and Remote Sensing, 40*(11), 2375–2383. https://doi.org/10.1109/TGRS.2002.803792

Casu, F., Manzo, M., & Lanari, R. (2005). Performance analysis of the SBAS algorithm for surface deformation retrieval. Proceedings of the Fringe 2005 Workshop, 28 November–2 December 2005, Frascati, Italy. Available online: http://earth.esa.int/fringe2005/proceedings/papers/483_lanari.pdf

Casu, F., Manzo, M., & Lanari, R. (2006). A quantitative assessment of the SBAS algorithm performance for surface deformation retrieval. *Remote Sensing of Environment*. *102*(3–4), 195–210. https://doi.org/10.1016/j.rse.2006.01.023

Chen, C. W., & Zebker, H. A. (2001). Two-dimensional phase unwrapping with the use of statistical models for cost functions in nonlinear optimization. *Journal of the Optical Society of America A, 18*(2), 338–351. https://doi.org/10.1364/JOSAA.18.000338

Crosetto, M., Crippa, B., Biescas, E., Monseratt, O., Aguno, M., & Fernandez, P. (2005). Land deformation monitoring using SAR interferometry: state-of-the-art. *Photogrammetrie, Fernerkundung und Geoinformation*. *6*, 497–510.

Crosetto, M., & Pasquali, P. (2008). DSM generation and deformation measurement from SAR data. In: Li, Z., Chen, J., Baltsavias, E. (Eds) (2008). *Advances in Photogrammetry, Remote Sensing and Spatial Information Sciences* (pp. 157–167). 2008 ISPRS Congress Book. Leiden, The Netherlands, CRC Press.

ESA (2020). Sentinel online. https://sentinel.esa.int/web/sentinel/home

Ferretti, A., Prati, C., & Rocca, F. (2000). Nonlinear subsidence rate estimation using permanent scatterers in differential SAR interferometry. *IEEE Transaction on Geoscience and Remote Sensing. 38*(5), 2202–2012. https://doi.org/10.1109/36.868878

Ferretti, A., Prati, C., & Rocca, F. (2001). Permanent scatterers in SAR interferometry. *IEEE Transaction on Geoscience and Remote Sensing, 39*(1), 8–20. https://doi.org/10.1109/36.898661

Goel, K. & Adam, N. (2014). A Distributed Scatterer Interferometry Approach for Precision Monitoring of Known Surface Deformation Phenomena. *IEEE Transaction on Geoscience and Remote Sensing, 52*(9), 5454–5468. https://doi.org/10.1109/TGRS.2013.2289370

Hanssen, R. F. (2001). *Radar interferometry: Data interpretation and error analysis* (vol. 2). Dordrecht, The Netherlands: Kluwer Academic, 2001.

Krieger, G., Moreira, A., Fiedler, H., Hajnsek, I., Werner, M., Younis, M., Zink, M. (2007). TanDEM-X: A satellite formation for high-resolution SAR Interferometry. *IEEE Transaction on Geoscience and Remote Sensing, 45*(11), 3317–3341. https://doi.org/10.1109/TGRS.2007.900693

Lanari, R., Lundgren, P., Manzo, M., & Casu, F. (2004). Satellite radar interferometry time series analysis of surface deformation for Los Angeles, California. *Geophysical Research Lett*ers, *31*, L23613. https://doi.org/10.1029/2004GL021294

Lanari, R., Casu, F., Manzo, M., Zeni, G., Berardino, P., Manunta, M., & Pepe, A. (2007). An overview of the Small Baseline Subset Algorithm: A DInSAR technique for surface deformation analysis. *Pure and Applied Geophysics*, *164*, 637–661. https://doi.org/10.1007/s00024-007-0192-9

Lee, C-W., Lu, Z., Jung, H-S., Won, J-S., & Dzurisin, D. (2006). Surface deformation of Augustine Volcano, 1992–2005, from Multiple-Interferogram processing using a refined Small Baseline Subset (SBAS) Interferometric Synthetic Aperture Radar (InSAR) Approach. In Power, J. A., Coombs, M. L., & Freymueller, J. T., (eds). *The 2006 eruption of Augustine Volcano, Alaska*. *U.S. Geological Survey Professional Paper* 1769.

Normand, J. C. L. & Heggy, E. (2015). InSAR assessment of surface deformations in urban coastal terrains associated with groundwater dynamics. *IEEE Transaction on Geoscience and Remote Sensing. 53*(12), 6356–6371. https://doi.org/10.1109/TGRS.2015.2437368

Rabus, B., Eineder, M., Roth, A., Bamler, R. (2003). The Shuttle Radar Topography Mission—A new class of digital elevation models acquired by spaceborne radar. *ISPRS Journal of Photogrammetry and Remote Sensing*, *57*(4), 241–262. https://doi.org/10.1016/S0924-2716(02)00124-7

Robert, M., & Norton, R. M. (1984). The double exponential distribution: Using calculus to find a maximum likelihood estimator. *The American Statistician. American Statistical Association*, *38*(2), 135–136

Rosen, P. A., Hensley, S., Junghin, I. R., Li, F. K., Madsen, S. N., Rodriguez, E., & Goldstein, R. M. (2000). Synthetic Aperture Radar Interferometry. *Proceedings of the IEEE*, *88*(3), 333–382. https://doi.org/10.1109/5.838084

Sandwell, D. R., Mellors, X., Wei, T., M., & Wessel, P. (2011). Open radar interferometry software for mapping surface deformation. *Eos*, *92*(28), 234–235. https://doi.org/10.1029/2011EO280002

Schwind, M., Schneider, G., Palubinskas, T., Storch, R., Muller, R., & Richter, R. (2009). Processors for ALOS optical data: Deconvolution, DEM generation, orthorectification, and atmospheric correction. *IEEE Transaction on Geoscience and Remote Sensing, 47*(12), 4074–4082. https://doi.org/10.1109/TGRS.2009.2015941

Tadono, T., Nagai, H., Ishida, H., Oda, F., Naito, S., Minakawa, K., & Iwamoto, H. (2016). Generation of the 30 m-mesh global digital surface model by ALOS PRISM. *International Archives of Photogrammetry and Remote Sensing and Spatial Information Sciences*, *XLI*(B4), 157–162. https://doi.org/10.5194/isprs-archives-XLI-B4-157-2016

Yilmaz, A., & Erdoğan, M. (2018). Designing High-Resolution Countrywide DEM for Turkey. *International Journal of Engineering and Geosciences*, *3*(3), 98–107. https://doi.org/10.26833/ijeg.384822